Critical condition for initiation of dynamic recrystallisation in electron beam powder bed fused Ti-6Al-4V Alloy

Original
Critical condition for initiation of dynamic recrystallisation in electron beam powder bed fused Ti-6Al-4V Alloy / Taghian, M., Mani, H., Mosallanejad, M., Abdi, A., Saboori, A., Iuliano, L.. - In: JOURNAL OF ALLOYS AND COMPOUNDS. - ISSN 0925-8388. - 1005:(2024). [10.1016/j.jallcom.2024.176165]

Publisher:
ELSEVIER SCIENCE SA

Published
DOI:10.1016/j.jallcom.2024.176165

Journal of Alloys and Compounds 1005 (2024) 176165

Contents lists available at ScienceDirect

Journal of Alloys and Compounds

journal homepage: www.elsevier.com/locate/jalcom

Critical condition for initiation of dynamic recrystallisation in electron beam powder bed fused Ti-6Al-4 V Alloy

Mohammad Taghian [a], Hossein Mani [b], Mohammadhossein Mosallanejad [a], Ata Abdi [c], Abdollah Saboori [a,*], Luca Iuliano [a]

[a] *Integrated Additive Manufacturing Center, Department of Management and Production Engineering, Politecnico di Torino, Corso duca degli Abruzzi, Torino 10129, Italy*
[b] *Department of Materials Engineering, Isfahan University of Technology, Isfahan 84156–83111, Iran*
[c] *Faculty of Materials Science and Engineering, K.N. Toosi University of Technology, Tehran 19395-1999, Iran*

ARTICLE INFO

Keywords:
Additive manufacturing
Electron beam powder bed fusion
Ti64
Thermomechanical processing

ABSTRACT

Despite the unique capabilities of Additive Manufacturing (AM) processes for producing Ti components with complex geometries, the desired properties are only achievable if a holistic scheme is devised, considering the synergistic role of post-processing steps. This work aimed to enhance the applicability of metal AM products by improving the process chain in the manufacturing industry. For this purpose, the current work demonstrates a comprehensive investigation into the hot deformation of Ti-6Al-4 V (Ti64) pre-forms produced via the Electron Beam Powder Bed Fusion (EB-PBF) process focusing on the determination of critical conditions for initiating Dynamic Recrystallization (DRX) in these components. Following a sequential evaluation procedure, hot deformation experiments were carried out at temperatures ranging from 1000 to 1200 °C and strain rates of 0.001–1 s^{-1} to determine the critical stress and strain required for initiating DRX in Ti64 pre-forms and compare them to their wrought counterparts. In addition, a specific Finite Element Model (FEM) was coupled with DRX kinetics equations to predict the volume percentage of DRX grains during the hot deformation of the pre-forms. The analysis of flow stress curves showed a significant peak stress at low strains, which is then followed by a period of flow softening and eventually transitions into a nearly steady-state flow at higher strains. In addition, compared to their wrought counterparts, the EB-PBF samples exhibited a significantly superior flow softening behavior, as evidenced by a more significant volume fraction of DRX and faster recrystallisation rates. It was also revealed that the normalised strain for DRX initiation in the EB-PBF Ti64 and wrought one was 0.55 and 0.67, respectively. FEM results closely matched the experimental finding, confirming its reliability in providing valuable insights into microstructural evolution and offering a time-efficient alternative for process design and property optimisation, lowering dependence on trial-and-error approaches. Through a combination of experiments, numerical analysis, and finite element simulations, this study sheds light on the macroscopic deformation and microstructural transformations occurring during hot working processes.

1. Introduction

Ti-6Al-4 V (Ti64), an $\alpha + \beta$ titanium alloy, has attracted widespread attention in various sectors, most notably in the aerospace and biomedical fields, owing to its exceptional properties [1–3]. Its low density, combined with a high strength-to-weight ratio, superior corrosion resistance, improved fatigue resistance, and biocompatibility, position it as a material of choice for various applications [4–6]. The versatility of Ti64 alloy has led to its adoption in industries that demand the highest levels of reliability and performance [7].

Traditionally, the manufacturing of Ti64 parts has relied on processes such as forging, involving the retrieval of titanium billets via the Kroll method, followed by alloying and shaping these billets utilising thermomechanical processes [8–10]. Despite being effective, this conventional route is inefficient and costly [11]. In recent decades, efforts have been made to improve production efficiency and reduce expenses by addressing the inherent difficulties associated with titanium alloys, including their low thermal conductivity and high reactivity with oxygen [12–14]. In this context, AM has emerged as a revolutionary solution, offering a more efficient and cost-effective way for Ti component

---

* Corresponding author.
E-mail address: abdollah.saboori@polito.it (A. Saboori).

https://doi.org/10.1016/j.jallcom.2024.176165
Received 30 April 2024; Received in revised form 12 August 2024; Accepted 25 August 2024

production while tackling the limitations of traditional methods.

Through a layer-by-layer construction approach, utilising metal powders and Computer-Aided Design (CAD) files, AM technologies have revolutionised the manufacturing of complex-shaped components [15–17]. Among AM processes, Electron Beam Powder Bed Fusion (EB-PBF) has shown significant promise for Ti64 parts. Its unique working conditions, including high vacuum and preheating steps, reduce residual stresses, increase powder recyclability, and improve purity [18,19].

However, the advancement of AM technologies in fabricating Ti64 components has not been without challenges, including microvoids and microstructural inhomogeneities [20]. To overcome these issues, post-processing methods like Hot Isostatic Pressing (HIP) and controlled forging have become indispensable, aiming for a refined duplex microstructure that merges the advantages of lamellar and globular structures for superior properties [21].

This quest for perfection continues, as the AM field still faces challenges such as microvoids and microstructural inhomogeneities [21]. HIP and controlled forging have been recognised as essential post-processing techniques to address these issues. These processes refine the microstructure and play a pivotal role in improving the mechanical characteristics of parts, leveraging both lamellar and globular microstructures to attain ideal material properties. The merging of AM with subsequent thermomechanical treatments marks a research frontier aimed at unlocking the full potential of the Ti64 alloy [22].

In the pursuit of understanding and improving the production and processing of Ti64, DRX emerges as a key mechanism in modulating microstructure and mechanical properties [23]. It is well documented that identifying the DRX initiation point is crucial during hot industrial processing, as it significantly affects the atomic structure of alloys, mechanical strength, and behavior at elevated temperatures. It is well-reported that alloy composition, deformation conditions, and initial grain size influence the initiation of DRX [24–26].

Research has suggested that a stress peak occurring at a consistent strain rate may signal the initiation of dynamic recrystallization (DRX). This inflection point, linked to a change in the thermodynamic state of the system, highlights the critical condition for the onset of DRX [27]. The Poliak-Jonas method, which uses a third-order polynomial fit to the strain hardening-stress relationship, provides insight into DRX initiation and the dynamic interaction between stress and microstructural evolution [28,29].

This research explores the hot deformation and microstructural transformation of EB-PBF Ti64 alloys, focusing on different temperatures and strain rates to determine the critical conditions for DRX initiation. This study also integrates DRX kinetics into a finite element model tailored for EB-PBF Ti64 specimens. The goal is to predict the proportion of DRX during hot compression tests, thereby improving the understanding of the hot workability of EB-PBF samples compared to conventional production methods for the Ti64 alloy. Additionally, this work proposes a novel simplified flow stress model for EB-PBF materials, addressing a fundamental gap in the current understanding of the deformation of additively manufactured alloys.

2. Materials and methods

2.1. Characterisation

The Ti64 powder morphology was analysed using SEM, while its cross-section was assessed using an Optical Microscope (OM). Subsequently, to prepare the as-deformed samples for microstructural analysis, they were cut from the central part (along the build direction) and ground down using 2400 grit SiC abrasive paper. All the as-ground samples were polished with 1 μm diamond paste and silica suspension. The polished samples were then etched using the Kroll etchant solution composed of 92 ml H_2O, 6 ml HNO_3, and 2 ml HF [30].

2.2. Sample preparation

The cylindrical specimens employed in this research were produced utilising Ti64 powder of extra-low interstitials (ELI) grade. The raw material used was spherical powder, produced via plasma atomisation with a particle size distribution of 45–106 μm. Scanning Electron Microscopy (SEM) analysis of the virgin powder showed that all the particles are spherical with smooth external surfaces that include a few satellites (Fig. 1(a-b)). Fig. 1(c) confirms that no internal porosity is presented in the feedstock material.

Table 1 compares the chemical composition of the starting powder and the wrought material, which served as the reference alloy for this analysis. The table indicates that the initial powder is characterised by low concentrations of carbon, nitrogen, oxygen, and iron.

Cylindrical Ti64 parts for hot compression tests were produced using an Arcam A2X EBM machine. The production process adhered to the standard Arcam A2X built theme for Ti64, employing a 60 kV accelerating voltage, 50 μm layer thickness, and software version 5.2.52. During the EB-PBF process, 25 mA and 200 μm were used as focus and line offsets, respectively. Vertical cylinders with dimensions of Φ=10 mm and h=15 mm were manufactured directly on a stainless steel start plate with a thickness of 10 mm. The preheating temperature for the start plate was 700 °C, whereas, throughout the EB-PBF process, the powder bed temperature was higher than 580 °C.

Hot deformation experiments were conducted using a Zwick Roell Z250 universal machine equipped with a load frame capable of supporting 250 kN of force. To maintain the set temperatures, an automated resistance furnace was employed, offering a temperature precision of ±5 °C. Load and displacement data were recorded during the tests using a data collecting system, which also recorded the load and displacement data. The hot compression experiments were conducted in the single-phase β region, with temperatures between 1000 and 1200 °C and temperature increments of 50 °C. The as-built and wrought specimens were kept at the deformation temperature for 10 minutes before the compression test. Various strain rates between 0.001 and 1 s^{-1} were applied, resulting in a total strain of 0.70 % (Fig. 2). A thin layer of mica was placed between specimens and anvils to minimise sticking issues, ensure consistent compression forces, and reduce friction. Following each hot compression test, the deformed sample was promptly quenched in water to retain its as-deformed microstructure.

3. Results and discussion

3.1. Starting microstrucutres

A comparative analysis of the microstructures of the Ti64 alloy manufactured using EB-PBF and its conventionally wrought counterpart is illustrated in Fig. 3(a-b). The microstructure of the EB-PBF Ti64 alloy, shown in Fig. 3(a), is characterised by the presence of vertically oriented, long columnar β grains, known as the Build Direction (BD), in addition to a lamellar structure of α phases. Moreover, it is observed that while the EB-PBF Ti64 sample includes several colonies exhibiting parallel platelets of the α phase, the majority of the α laths remain isolated. This characteristic may result from the rapid cooling rate experienced during phase transformation. A consistently thin α grain boundary layer is observed along the former beta grains.

In contrast, the wrought Ti64 alloy exhibits a duplex α+β microstructure, as depicted in Fig. 3(b). The mean size of the grains in this alloy is 52 ± 5 μm. The bright areas denote the β phase, while the dark matrix corresponds to the α phase.

Fig. 3 confirms that the microstructure of the as-built EB-PBF and as-received Ti64 samples are different, which can directly affect their mechanical response at high temperatures, resulting in different flow softening behaviour in both samples [31,32]. Hence, this study investigates the flow softening behavior of the as-built EB-PBF samples, with a particular emphasis on the kinetics of DRX and the identification

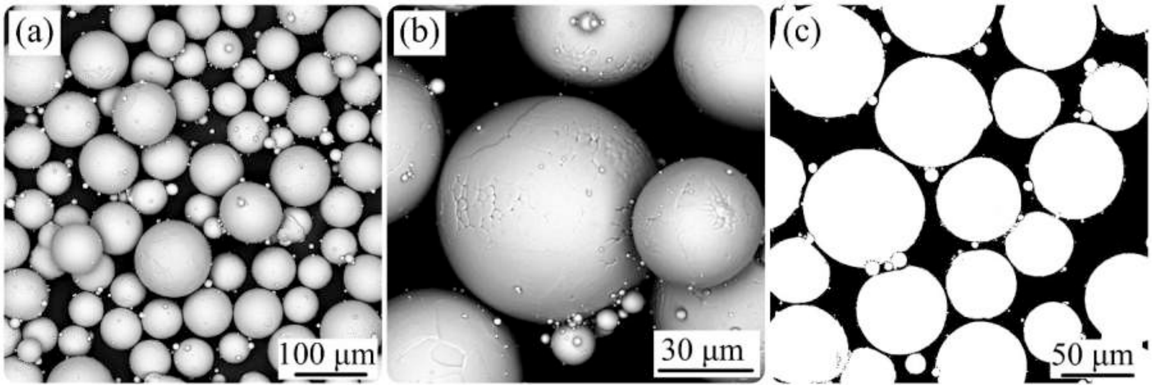

Fig. 1. (a,b) SEM images, and (c) cross-section view via OM of the powder used in this work.

Table 1
Initial powder and benchmark alloy chemical compositions utilised in this study.

	Ti	Al	V	Fe	C	N	O	H
Arcam ELI (wt%)	Bal.	6.38	3.86	0.18	0.02	0.01	0.08	0.002
Wrought (wt%)	Bal.	6.22	4.13	0.21	0.01	0.01	0.11	0.001
Standard ELI (wt%)	Bal.	5.50–6.50	3.50–4.50	<0.25	<0.08	0.05	<0.13	<0.012

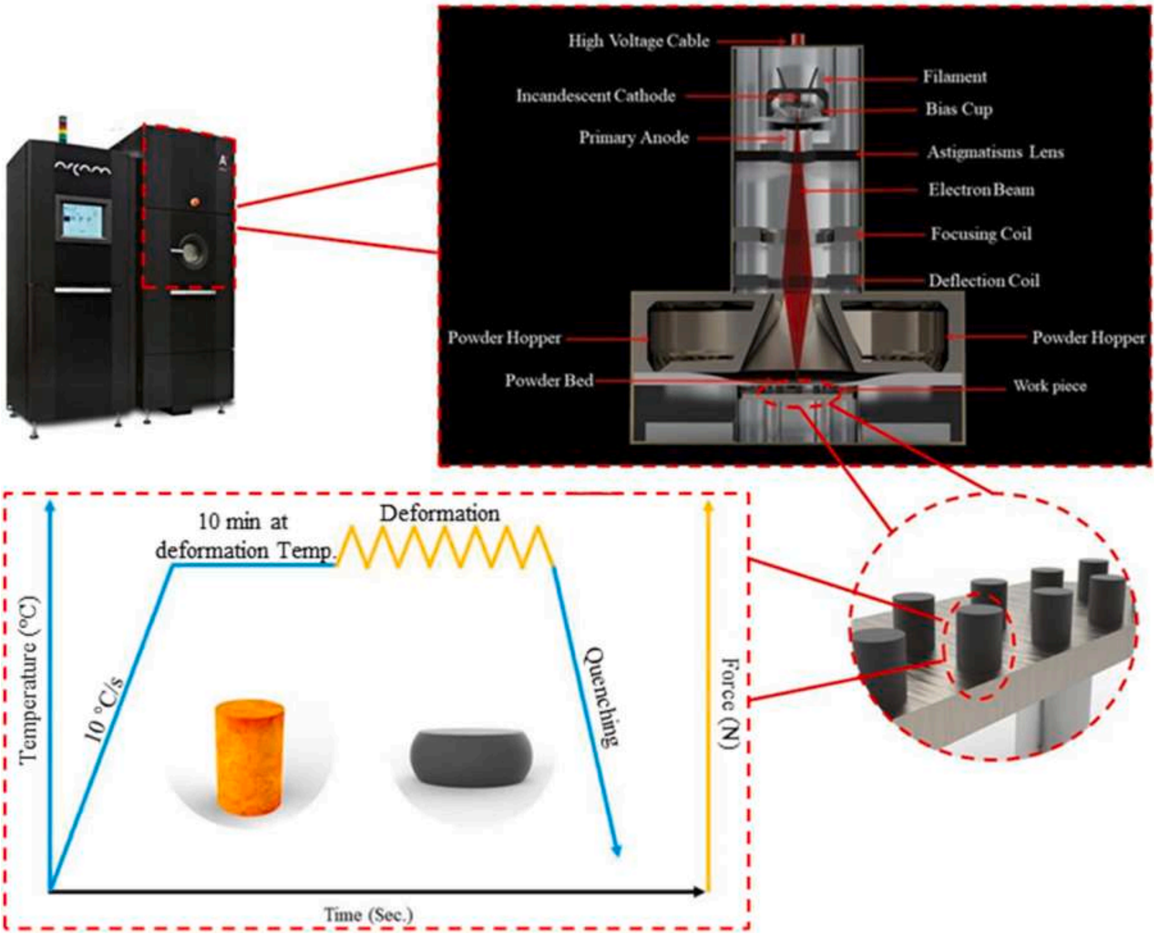

Fig. 2. Schematic of different stages of the process.

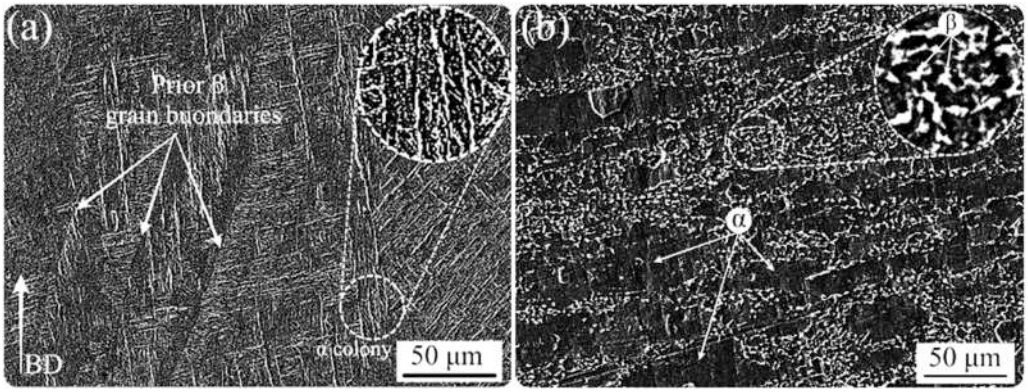

Fig. 3. SEM images of (a) the as-built EB-PBF and (b) the as-received wrought Ti64 samples used in this study.

of critical conditions required to initiate DRX

3.2. *Curve corrections*

During hot compression testing, the frictional effects between the anvils and the sample surface have been well documented [31,33]. Therefore, this frictional force, which can significantly impact the stress curves, should be considered during data analysis to minimise its detrimental effects. Hence, the upper-bound theory, which provides a foundational analytical assessment of the cylinder compression test, was applied in the current study to ascertain the constant friction factor (m) [34,35]. Fig. 4 shows the friction-corrected and main stress-strain curves of an EB-PBF sample at a strain rate of 0.1 s^{-1} and temperature of 1200°C, comparatively. As evident in Fig. 4, which is a representative curve, the friction during the hot compression leads to higher flow stresses, particularly at higher strains. In this study, sample surface-anvil friction was addressed for accurate flow softening curve analysis. Subsequently, all stress-strain curves were corrected accordingly.

According to the literature, stress peaks in stress-strain curves indicate the occurrence of DRX in the material [33]. While this phenomenon is commonly observed in several materials, it is acknowledged that well-defined peaks may not always be present in some materials. Therefore, further evaluations are needed to determine the initiation of DRX. For instance, Poliak and Jonas [28,29,36] demonstrated that inflections in the work hardening rate (θ) as a stress function could effectively indicate the initiation of DRX. Building upon their seminal work, Najafizadeh and Jonas [27] refined the approach by simplifying the determination of work hardening by deriving true stress with respect to true strain.

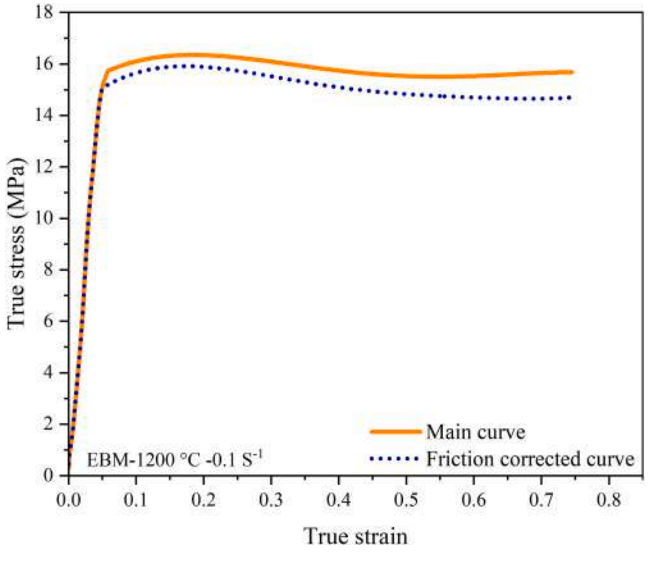

Fig. 4. Comparison of stress-strain curves for an EB-PBF sample at 1200°C and a strain rate of 0.1 s^{-1}, including friction-corrected and original data.

However, calculating such derivatives can be very challenging, mainly owing to the inherent short-range fluctuations in the flow curves. Therefore, to mitigate the impact of these fluctuations, a high-order polynomial fitting technique should be employed to eliminate noise and variations, thereby enhancing the consistency of the stress-strain curves [37]. For this reason, all stress-strain curves in this study first underwent friction correction to account for the significance of friction during the experimental procedure. Subsequently, a sophisticated sixth-order polynomial function was applied to precisely fit and smooth the friction-corrected curves.

Fig. 5(a-b) illustrates the true stress-strain graphs derived from the EB-PBF and wrought samples in their as-built state. These curves provide valuable insights into the influence of hot deformation under varying temperatures and strain rates. Notably, the data shows a decrease in flow stress with increasing deformation temperature, indicating that higher temperatures improve material flow during deformation, leading to increased mobility that can aid processes like DRV and DRX. The DRV and DRX occur due to increased flow softening, resulting in decreased work hardening, the ultimate tensile strength (UTS), toughness, and critical stress and strain of the DRX. Reducing the strain rate typically lowers the UTS and work hardening because it allows for increased movement of dislocations and dynamic recovery. However, it should improve the material toughness, but it decreases due to a decrease in the UTS point. In addition, the critical strain and stress for DRX decreases. These effects are vital for optimizing material properties in processes such as hot working.

Furthermore, comparing Fig. 5(a) and (b) provides further insights into the difference in flow stress between the EB-PBF and wrought samples. As the deformation temperature increases and the strain rate decreases, the difference in flow stress decreases. This phenomenon can be attributed to the higher diffusion rates observed at elevated temperatures, facilitating improved material homogeneity and reducing residual stresses caused by different processes used to create initial samples. These findings underscore the potential for optimising deformation conditions to align the mechanical properties of EB-PBF-produced samples with those of wrought counterparts.

Moreover, it is evident in Fig. 5(a, b) that the EB-PBF alloy exhibits a lower flow stress compared to the wrought alloy across all deformation conditions. This difference may be attributed to the distinct coefficient factors of the two sample types, which result from the rapid solidification and subsequent cooling during the AM process, resulting in metastable microstructures [38]. The difference in flow stress can also be attributed to other factors, including the initial microstructure of the samples, the presence of defects, and oxygen content. Although the EB-PBF samples exhibited a lower oxygen concentration than the

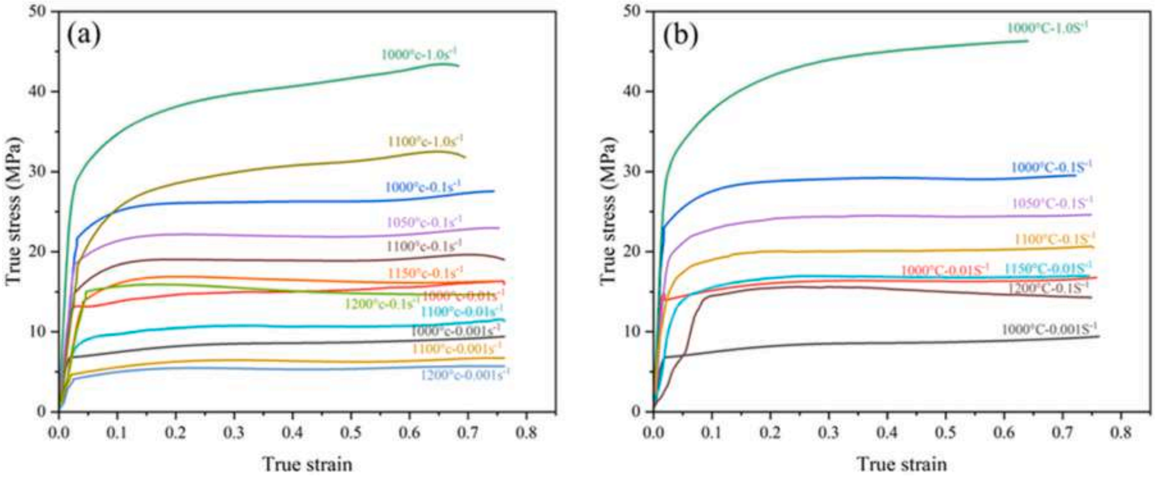

Fig. 5. Stress-strain plots for (a) as-built EB-PBF and (b) wrought Ti64 samples.

wrought material, they showed higher porosity (Table 1). Importantly, no macro porosity was detected in any of the plastically deformed samples at high temperatures. Consequently, compared to the wrought samples, the EB-PBF ones may exhibit a more effortless flow-softening behavior, which can prove advantageous for producing pre-forms using this method. The lower initial oxygen content in the EB-PBF sample (Table 1) significantly impacts its flow-softening behavior during the hot compression process. Higher oxygen levels increase strength and hardness but reduce ductility, making the material more brittle. Oxygen can inhibit dynamic recrystallisation (DRX) by pinning grain boundaries, leading to less effective flow softening. It also stabilises the alpha phase, which is harder and less deformable [1].

The localised melting and rapid cooling resulting from the rapid solidification process in the EB-PBF lead to a higher density of dislocations compared to wrought samples. A higher volume fraction of the β phase in the initial microstructure of EB-PBF samples (Fig. 3) enhances flow softening. This is achieved by facilitating dynamic recovery and recrystallization, promoting phase transformations during deformation, and reducing overall flow stress due to the lower flow stress of the β phase compared to the α phase.

The stress-strain curves are accurate sources for evaluating the occurrence of DRV and DRX mechanisms [2,3]. Specifically, peak stress is an important indicator of the DRX mechanism. This is characterized by a rapid increase in flow stress to a peak value at the beginning of compression due to significant work hardening (WH) and minimal DRV and DRX. Subsequently, the flow stress gradually decreases to a steady value, indicating a balance between WH and DRX, which is maintained until the end of compression. Conversely, for the DRV mechanism, the flow stress rapidly increases to a saturation value at the beginning of compression, again due to significant WH and minimal DRV.

It is evident from Fig. 5 that, throughout the entire temperature range, all curves attain a steady state when the strain rate falls below 0.1 s^{-1}. This behavior suggests that the softening and work hardening rates are equally competitive across the entire temperature range. The observed flow softening behavior implies that at high strain rates, DRX, DRV, or superplasticity could potentially occur [39].

Quan et al. reported that, in the β phase, DRV could be considered dominant due to the BCC crystallographic structure with a high Stacking Fault Energy (SFE) [25]. Additionally, as shown in Fig. 5, DRX fluctuations and stress-strain curves, specifically those observed at elevated temperatures and reduced strain rates, may also be regarded as softening mechanisms. Dislocations created during the deformation of materials with a high SFE, such as Ti64, are initially impeded, followed by climbing and annihilation, resulting in the formation of subgrains within the grain interiors. Moreover, Seshacharyulu et al. documented that DRX is the prevailing softening mechanism in the β phase regime of the Ti64 alloy [40]. Consequently, additional research, particularly microstructure investigation, is necessary to determine the precise mechanisms that trigger hot deformation. Additionally, Ding et al. reported that dynamic recrystallisation occurs within the temperature range of 1000–1050 °C and at a strain rate of 0.1 s^{-1} for Ti64 alloy. Fig. 6 shows the observation of new β grains, which is considered evidence of dynamic recrystallisation, as reported by Ding et al. [41].

Fig. 6 presents the microscopic images of EB-PBF Ti64 samples resulting from hot deformation in the β region. The as-built EB-PBF Ti64 specimens displayed columnar grains aligned with the build direction (Fig. 6(a)). However, the hot deformed sample demonstrates evidence of recrystallisation, as indicated in the inset in Fig. 6(b). In the severe plastic deformation zone shown in Fig. 6(b), it is evident that some features of deformation are destroyed due to cooling across the transus temperature, but certain signs of dynamic recrystallisation (DRX) are still detectable. Specifically, irregular boundaries of prior β grains clearly indicate the occurrence of DRX. Additionally, the decrease in grain boundary size in the β region after hot compression, compared to its state before compression (primary columnar β region), further confirms the presence of DRX, as illustrated in Fig. 6.

3.3. *Constitutive modelling for DRX dynamic analysis*

The DRX model comprises two components: (i) the constitutive model for determining the DRX critical strain and (ii) the model for assessing the volume fraction of DRX. The DRX initiation was initially determined for both the wrought and EB-PBF samples. However, accurately determining the position of the inflection point is challenging because experimental errors are amplified during the fitting of the work hardening rate (θ) versus flow stress (σ) curve. This challenge arises from conducting experimental tests between 1000 and 1200 °C in the β region. In this region, as depicted in Fig. 5, the dynamic recrystallisation (DRX) is limited, which complicates the identification of peak stress [3]. To address this challenge, Poliak and Jonas [28,36] proposed a method using the partial derivative method to determine the location of the inflection point in the θ-σ curve. By effectively reducing the flow stress error introduced during the fitting process, this method facilitates the calculation of a critical strain with a higher level of accuracy. The process of derivation is described below:

$$\frac{\partial\theta}{\partial\sigma} = \frac{\partial\theta}{\partial\varepsilon}\bullet\frac{\partial\varepsilon}{\partial\sigma} = \frac{1}{\theta}\bullet\frac{\partial\theta}{\partial\varepsilon} = \frac{\partial(\ln\theta)}{\partial\varepsilon} \tag{1}$$

In this equation, the work hardening rate is denoted as θ, and the flow stress is defined as σ in MPa. Based on the findings of Poliak and Jonas, the initiation of DRX can be determined by identifying the

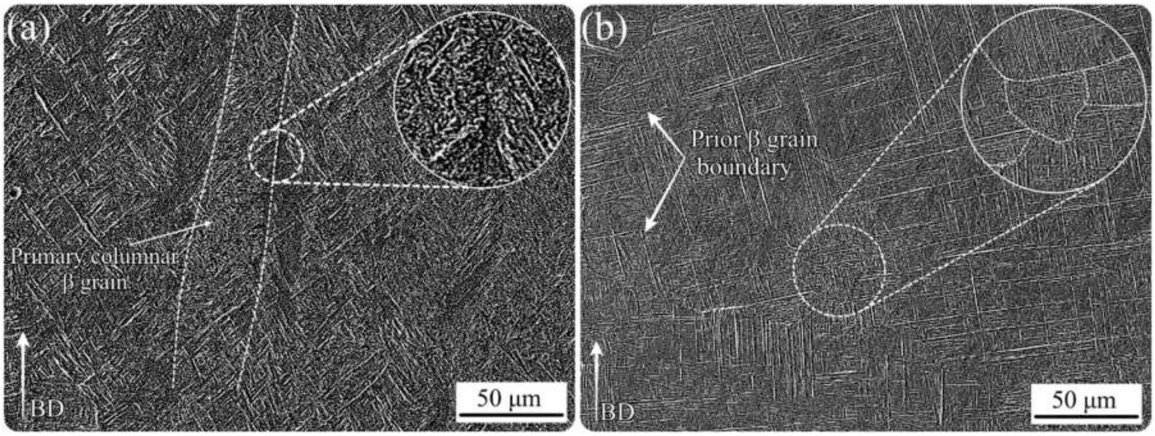

Fig. 6. EB-PBF Ti64 samples (a) before hot compression and (b) after hot compression at 1000 °C/0.1 s^{-1}.

inflection point in the $\ln(\theta)$-ε curve. Thus, it is possible to calculate the corresponding critical strain value (ε_c) by utilising the critical value of the $\partial(\ln(\theta)\text{-}\varepsilon)/\partial\varepsilon$ curve for various deformation strain rates and temperatures.

In this study, the $\ln(\theta)$-ε plots were subjected to curve fitting using third-order polynomials up to their maximum values. Fig. 7 compares the original $\ln(\theta)$-ε curve and its corresponding polynomial fit. It is evident from Fig. 7 that the third-order polynomial almost accurately fits the curve. Consequently, this fitting strategy was employed to determine the critical strain under various deformation conditions.

The critical strain for DRX initiation was calculated using the approach proposed by Najafizadeh and Jonas [27], which involved fitting all the curves with third-order polynomials. At the inflection point of the fitted curve, which represents the critical strain for DRX initiation, the second derivative becomes zero, as demonstrated in the following equations [27]:

$$\ln\theta = A\varepsilon^3 + B\varepsilon^2 + C\varepsilon + D \tag{2}$$

A, B, C, and D denote specific deformation circumstances. The second derivative of Eq.2 with respect to ε can be mathematically represented as:

$$\frac{d^2\ln(\theta)}{d^2\varepsilon} = 6A\varepsilon + 2B \tag{3}$$

The critical strain for the onset of DRX coincides with the inflection point, where the second derivative reaches zero. Thus:

$$6A\varepsilon_c + 2B = 0 \Rightarrow \varepsilon_c = \frac{-B}{3A} \tag{4}$$

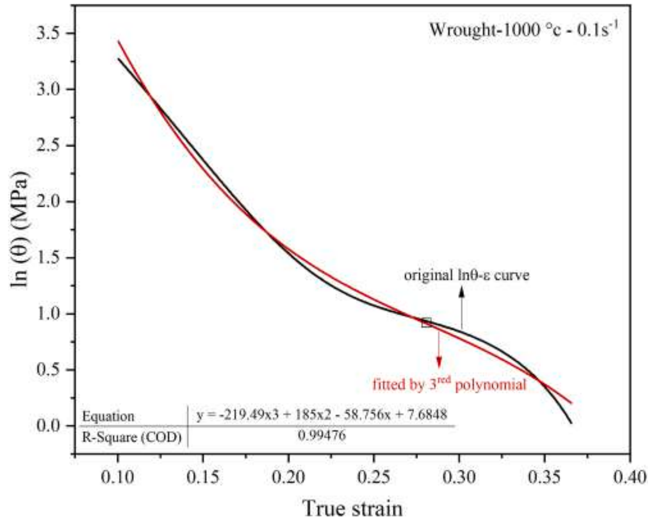

Fig. 7. An illustration of the ln(θ)-ε curve before and after being adjusted by a third-order fitting.

Following the same procedure, the critical conditions for initiation of DRX in all the experiments were determined, and the outcomes are presented for wrought and EB-PBF samples in Fig. 8.

The remarkable consistency in correlation factors validates the suitability of the inflection analysis for determining the critical condition necessary for the initiation of DRX. Therefore, the relationship between ε_c and ε_p can be derived using the following equation:

$$\varepsilon_c = a\varepsilon_p \tag{5}$$

As depicted in Fig. 8(a, b), the normalised critical strain values were 0.67 for the wrought sample and 0.55 for the EB-PBF sample. It is well-established that a lower normalised critical strain indicates an earlier onset of recrystallisation which was expected based on flow softening and DRX in EB-PBF and wrought samples. Therefore, it can be concluded that DRX occurs more rapidly in the EB-PBF sample than the wrought one, potentially due to the higher diffusion rate and probably the higher SFE in the EB-PBF structure. Consequently, the relative difference between ε_c and ε_p is smaller for the EB-PBF sample than for the wrought sample. The experimental ε_p can be expressed as a function of the Zener-Hollomon parameter. The correlations between ε_p and the Zener-Hollomon parameters for both wrought and EB-PBF samples are displayed in Fig. 9.

Also, ε_p can be written as a power function of the Zener-Hollomon parameter, as shown by the following equation:

$$\varepsilon_p = BZ^C \tag{6}$$

where B and C are material constants. Fig. 9 demonstrates the correlation involving the Z parameter and the peak strain, and the following equations for the wrought and EB-PBF samples can describe it:

$$\varepsilon_p^{Wrought} = 0.029Z^{0.13648} \tag{7}$$

$$\varepsilon_p^{EB-PBF} = 0.127Z^{0.05784} \tag{8}$$

Drawing upon the equations provided and considering the activation energy denoted by the slope of the $\ln(\varepsilon_p)$-$\ln(Z)$ plot, it can be inferred that the wrought material exhibits tremendous activation energy for the initiation of DRX than the EB-PBF samples.

A comparison of the equations reveals that as the strain rate increases and temperature decreases, the gap between the peak strain values of the wrought and EB-PBF samples widens due to the decrease in diffusion rate. This phenomenon can also be attributed to the higher SFE observed in EB-PBF samples compared to wrought ones, accelerating the

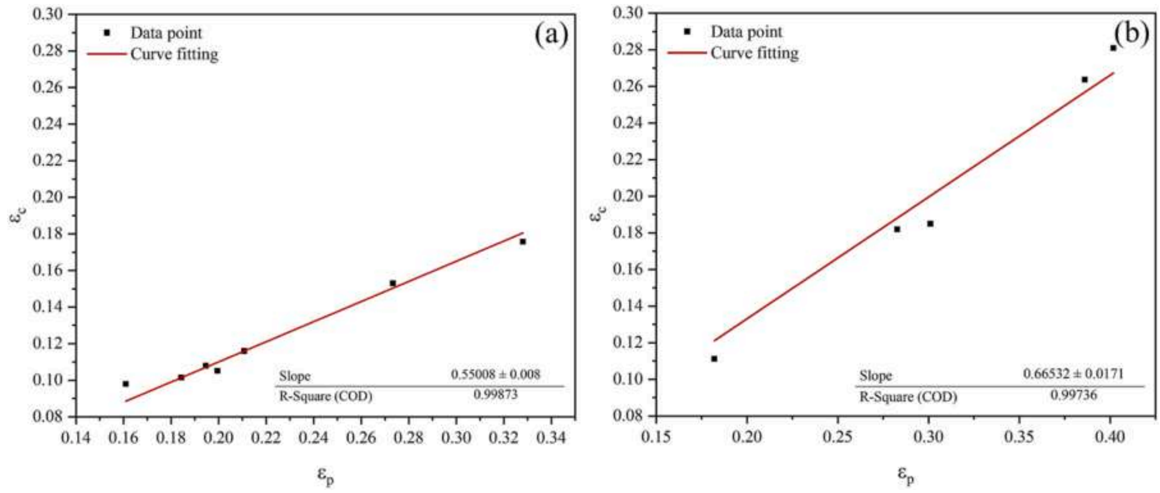

Fig. 8. Critical strain (ε_c) versus peak strain (ε_p) in different hot deformation conditions for)a) EB-PBF and)b) wrought samples.

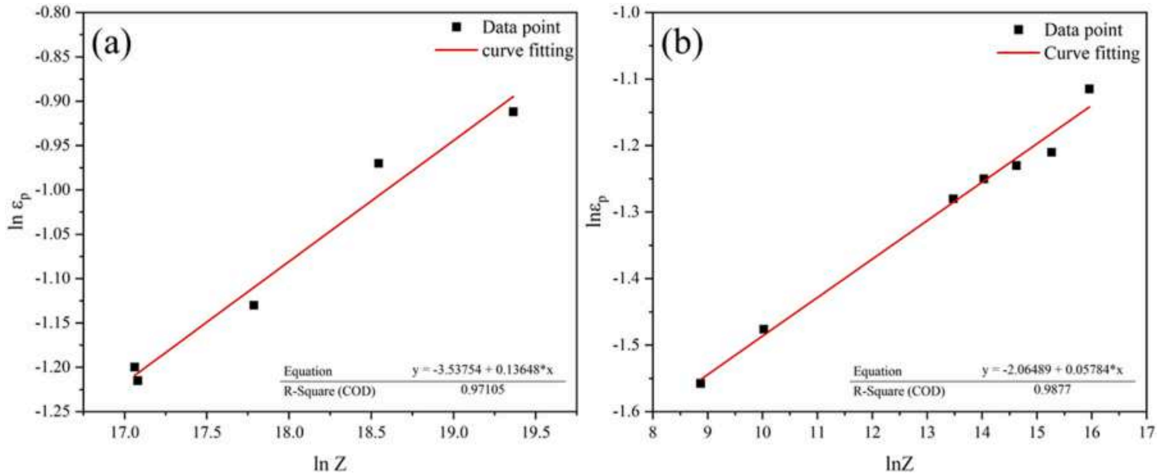

Fig. 9. Relationship between Z parameter and peak strain of (a) wrought and (b) EB-PBF.

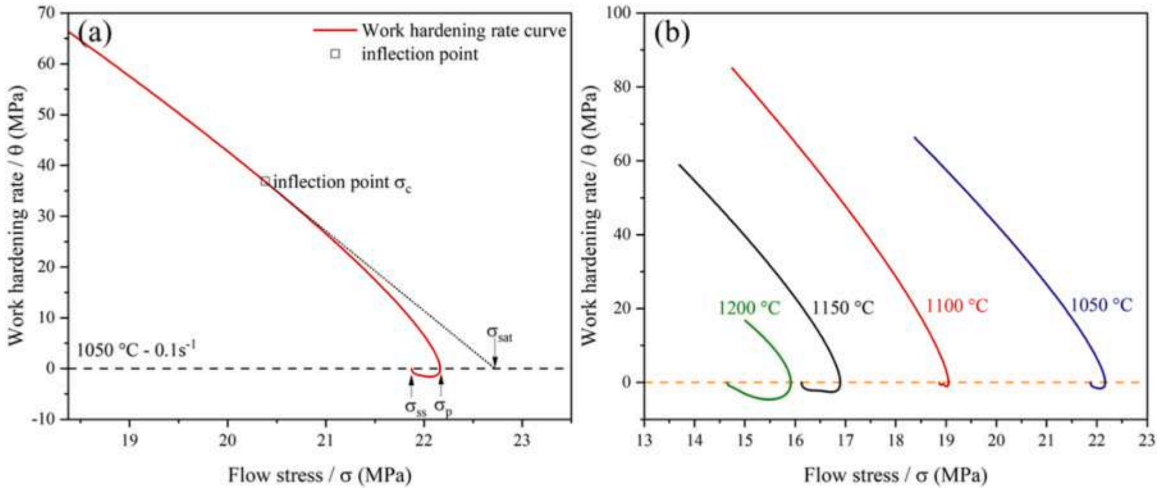

Fig. 10. (a) Steady-state stress and saturated stress at T=1050 °C and strain rate of 0.1 s^{-1} for EB-PBF samples, (b) work hardening rate versus flow stress curve in strain rate of 0.1 s^{-1} for T=1050 °C, T=1100 °C, T=1150 °C, T=1200 °C for EB-PBF samples.

initiation of work softening mechanisms.

3.4. DRX kinetic model from hot compression tests

The DRX volume fraction can be effectively modelled using the Johnson-Mehl-Avrami-Kolmogorov (JMAK) equation, which is widely used in studying recrystallisation kinetics. The DRX kinetic equation, based on the JMAK equation, is expressed as follows [25,42]:

$$X_{drx} = 1 - \exp\left[-\beta_d\left(\frac{\varepsilon - \varepsilon_c}{\varepsilon_{0.5}}\right)^{k_d}\right] \qquad (9)$$

where X_{drx} is the DRX volume fraction; $\varepsilon_{0.5}$ is the strain when the DRX volume fraction is 50 %, and β_d, k_d are material constants. Calculating the DRX volume percentage accurately under different deformation conditions and microstructures necessitates extensive and quantitative metallography measurements, which can be challenging. However, the true stress-strain curves associated with DRX provide valuable insights into the flow stress behavior of the metal during hot deformation, as influenced strongly by the microstructural changes. In addition to these measurements, Eq. 10 presents an alternative approach for determining the DRX volume fraction, offering another method to quantify the extent of the DRX volume fraction. which is not determined by the deformation condition (ε) in Eq. 9 and can only be calculated from the stress-strain curve obtained at a constant temperature and strain rate [43].

$$X_{drx} = \frac{\sigma_{sat} - \sigma}{\sigma_{sat} - \sigma_{ss}} \qquad (10)$$

The saturated stress is denoted as σ_{sat}, the steady-state test stress is σ_{ss}, and the actual stress of thermal deformation is defined as σ. Fig. 10 shows how to determine the steady-state, critical, peak, and saturation stress at 1050 °C with a strain rate of 0.1 s^{-1}.

It is worth noting that the point at which the work-hardening rate reaches zero corresponds closely to the peak stress in the flow stress curve. The steady-state stress can also be determined by identifying the second interception of the strain-hardening curve with the σ-axis. For this purpose, drawing a tangent line on the strain-hardening curve is necessary. The point where this tangent line intercepts and the σ-axis line represents the saturated stress.

By calculating σ_{sat} and σ_{ss} for each hot compression test, it is possible to determine the volume fraction of DRX at different strain rates and deformation temperatures using Eq. 10. The obtained DRX volume fraction can be fitted using software tools, as illustrated in Fig. 11. The strain at which 50 % DRX occurs under various deformation conditions is illustrated in Fig. 11(a), as determined by analysing this curve. Furthermore, Fig. 11(b-c) depicts the evolution of X_{drx} concerning strain, showcasing a sigmoidal trend. The values of $\varepsilon_{0.5}$ under different deformation conditions are summarised in Fig. 11(b). It is obvious that $\varepsilon_{0.5}$ rises with the strain rate between 0.01 and 0.1 s^{-1} and that $\varepsilon_{0.5}$ declined with the temperature increase within 1050–1200 °C.

The value of $\varepsilon_{0.5}$ should be determined for different deformation scenarios using Eq. 9. In order to accomplish this, X_{drx} needs to be plotted against strain [20]. However, the strain for 50 % of DRX ($\varepsilon_{0.5}$) depends on the strain rate and deformation temperature [20], which may be found using the same fitting method as the peak stress, as shown before, and is calculated as follows:

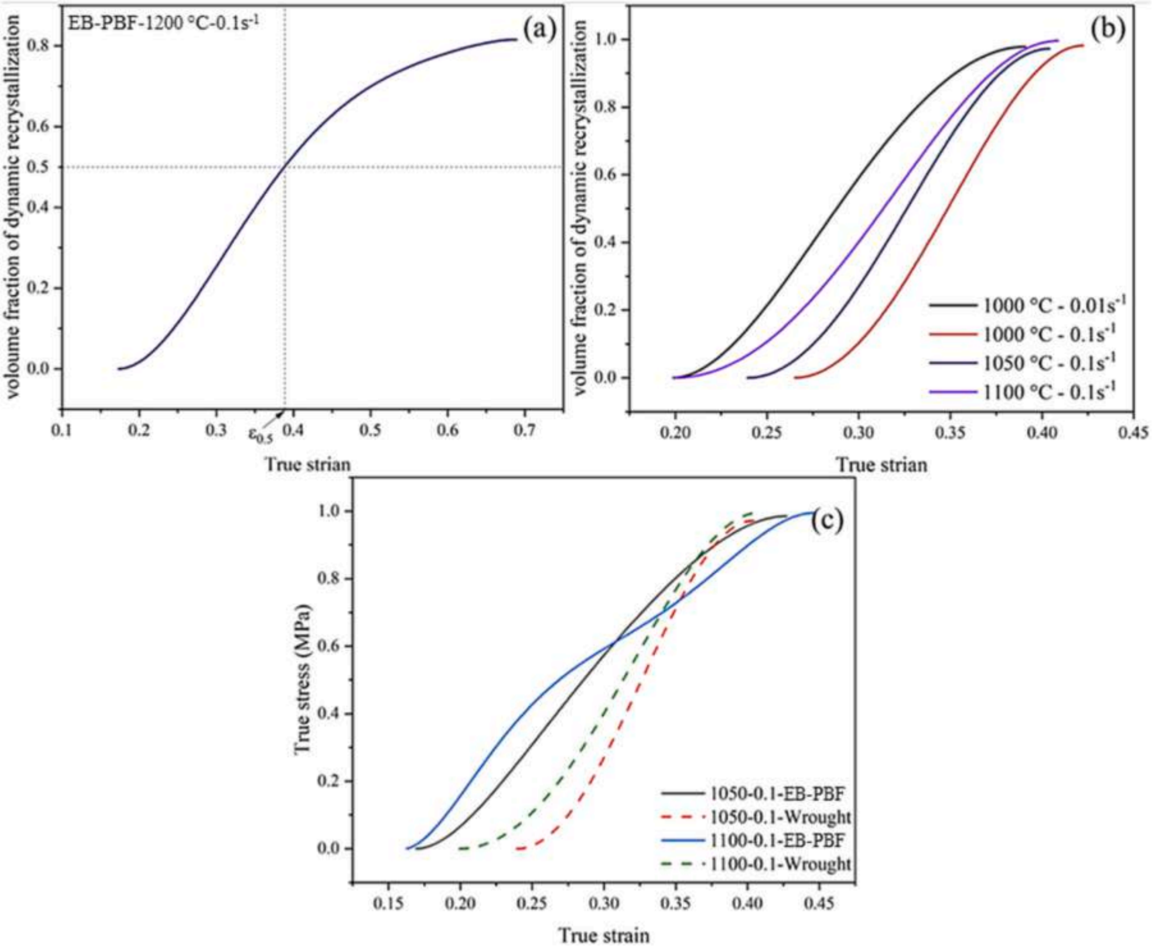

Fig. 11. Predicted volume fractions of DRX using Eq. 10 and true stress-strain curves (a) for 1200 °C and 0.1 s^{-1} of EB-PBF samples. (b) wrought samples. (c) two examples of EB-PBF and wrought samples.

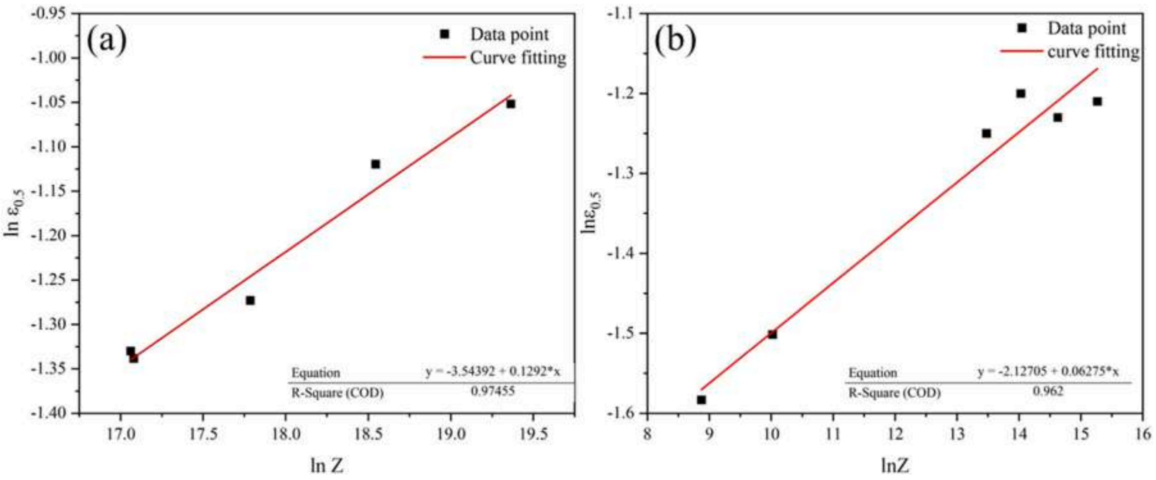

Fig. 12. The linear relationship between $\ln\varepsilon_{0.5}$ and lnZ for (a) wrought and (b) EB-PBF samples.

$$\varepsilon_{0.5} = DZ^{E} \tag{11}$$

where D and E are material constants, and Z is the Zener-Hollomon parameter. The linear relationships between $\ln(\varepsilon_{0.5})$ and $\ln(Z)$ under different hot compression tests were fitted, as shown in Fig. 12 for both EB-PBF and wrought samples, where the slope and intercept provide ln (E) and $\ln(D)$ through the linear fitting, respectively. The result of this calculation is presented as the following equations:

$$\varepsilon_{0.5}^{Wrought} = 0.029Z^{0.1292} \tag{12}$$

$$\varepsilon_{0.5}^{EB-PBF} = 0.11918Z^{0.06275} \tag{13}$$

To describe the evolution of X_{drx} based on strain, strain rate, and temperature using the JMAK equation, a natural logarithm is applied to both sides of Eq. 9:

$$\ln[-\ln(1 - X_{drx})] = \ln\beta_d + K_d \ln\frac{\varepsilon - \varepsilon_c}{\varepsilon_{0.5}} \tag{14}$$

Consequently, to determine β_d and K_d, $\ln[-\ln(1 - X_{drx})]$ is plotted versus $\ln\frac{\varepsilon-\varepsilon_c}{\varepsilon_{0.5}}$ (Fig. 13) using $\varepsilon_{0.5}$ and ε_c equations for both EB-PBF and wrought samples, using which K_d and $\ln(\beta_d)$ can be obtained by performing a linear fit.

Having calculated β_d and K_d, JMAK equation for DRX Kinetics were found for wrought and EB-PBF samples as follows:

$$X_{drx}^{Wrought} = 1 - \exp\left[-4.75\left(\frac{\varepsilon - \varepsilon_c}{\varepsilon_{0.5}}\right)^{1.81678}\right] \tag{15}$$

$$X_{drx}^{EB-PBF} = 1 - \exp\left[-3.4\left(\frac{\varepsilon - \varepsilon_c}{\varepsilon_{0.5}}\right)^{1.77103}\right] \tag{16}$$

It can be observed in Eqs. 15 and 16 that $1 \le K_d \le 2$ for both samples, which resembles one-dimensional growth according to JMAK analysis [44]. In contrast, the experimental evidence shows that the recrystallisation growth is not one-dimensional (Fig. 6b). Others have also verified this inconsistency [45], which is linked to recovery/recrystallisation interaction [46].

3.5. FEM Simulation of DRX

This study employs the 2D axisymmetric module in Abaqus/CAE 2022 software to visually evaluate the macroscopic deformation during the hot compression test. To accurately represent the material behaviour, flow stress data obtained from the hot compression tests were utilised to define the Ti6Al4V properties in Abaqus software, considering it as an isotropic hardening material for both EB-PBF and wrought samples. The material flow stress data is incorporated as discrete points within the plastic region of the material module. The software then automatically performs interpolation to generate a flow stress curve

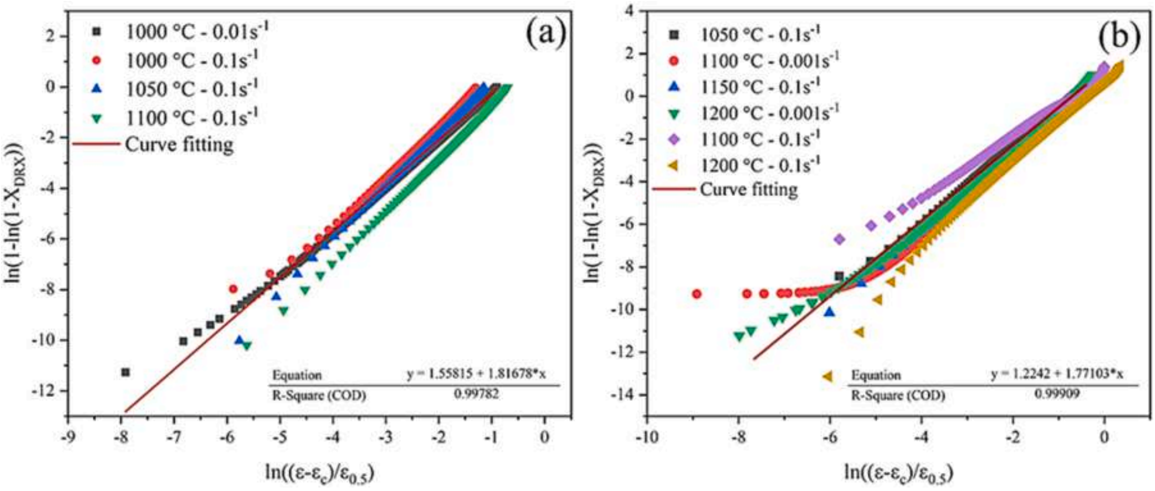

Fig. 13. The relationship between $\ln[-\ln(1 - X_{drx})]$ and $\ln\frac{\varepsilon-\varepsilon_c}{\varepsilon_{0.5}}$ at different deformation temperatures and strain rates for (a) wrought and (b) EB-PBF samples.

model that covers the behaviour of the material under different loading conditions. This allows the simulation to represent the mechanical response of the Ti6Al4V alloy accurately during hot compression.

In addition to the flow stress modelling, the recrystallisation volume fraction evolutions were investigated using the JMAK equations in the Abaqus software. These equations, implemented using the Fortran language and the USDFLD subroutine, allowed for the analysis of microstructural changes during thermo-mechanical transitions. Simulations were conducted at different temperatures, specifically 1000 °C, 1050 °C, and 1100 °C for both the EB-PBF model and the wrought samples. It is important to note that it was assumed that all points within the material would experience the same temperature during the simulation. This assumption aligns with the approach used in the hot compression tests, enabling consistent comparisons between the experimental and simulated results.

In all the simulations, the movement rate of the upper mold was set to 0.6 mm.s^{-1} in the initial state, and the simulation time was adjusted based on changes in the strain rate. The coefficient of friction between the mold and sample was determined using the Coulomb model, and a value of 0.1 was chosen through calculations. The elastic modulus and Poisson's ratio were assumed to be 200 GPa and 0.3, respectively, for both the EB-PBF and wrought modes. The standard solver and thermo-mechanical solution were employed in the simulation. A mesh size of 0.01 and the CAX4RT element type were used to ensure accurate results and minimise noise in the elements.

In this simulation, a quarter of the workpiece was modelled as symmetric and deformable, while the dominant part, the die, was represented as a discrete rigid body within the Abaqus environment. The dimensions of both parts were defined to resemble the experimental situation during the hot compression test.

3.5.1. Effect of deformation conditions on DRX

Figs. 14 and 15 show the simulated visualisations of the volume fraction of DRX. The figures depict different values of DRX volume fraction on the workpiece through colour distribution, where red denotes a complete DRX volume fraction. It is worth noting that the core metal remains unaffected by the inner wall friction, as it does not come into direct contact with the mold. The simulation results (Table 2) reveal significant recrystallisation in the central region, with a substantial recrystallised volume fraction. The average recrystallisation ratio for

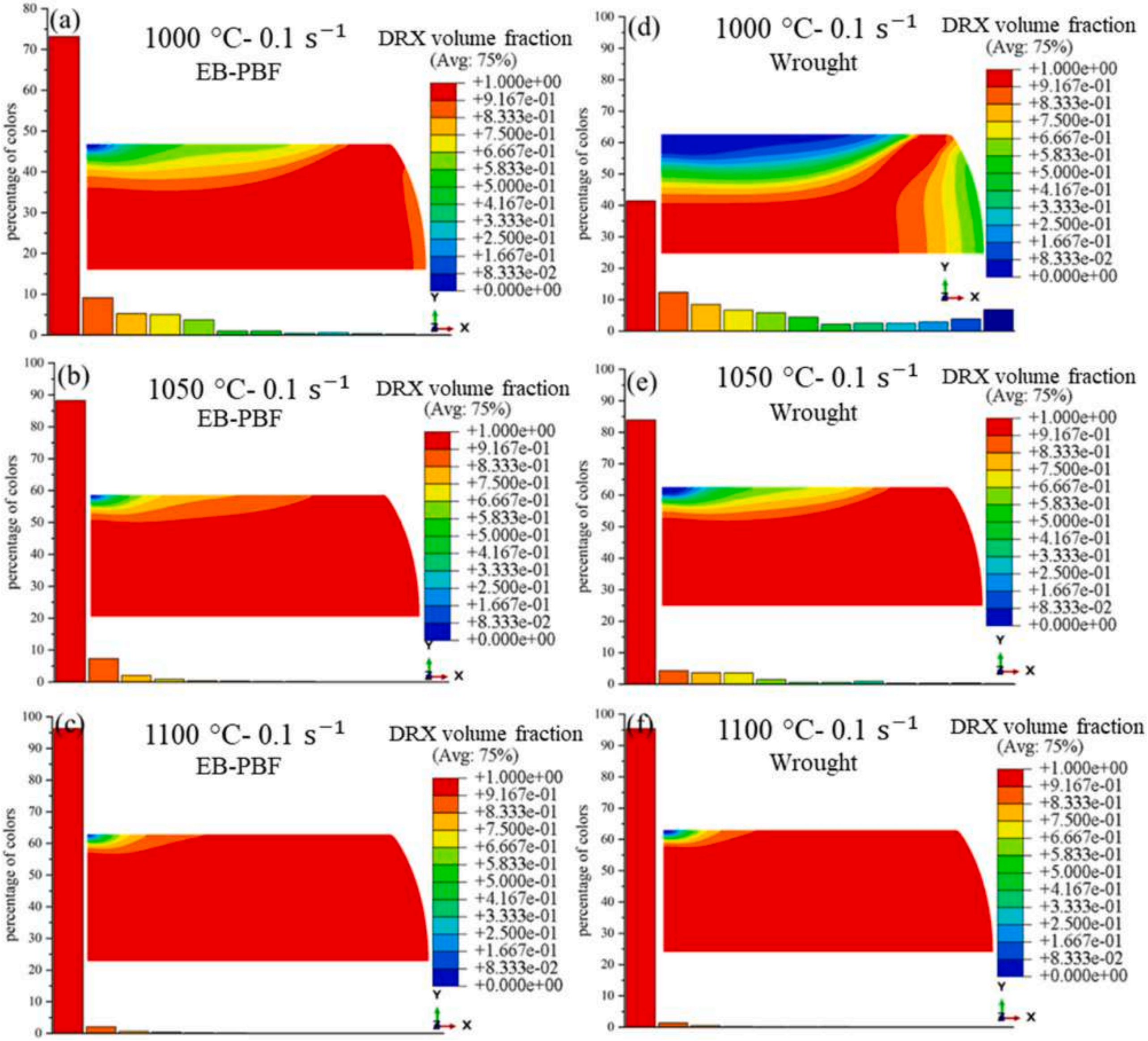

Fig. 14. DRX percentage distribution under a strain rate of 0.1s^{-1} and different temperatures: (a) T=1000°C; (b) T=1050°C; (c) T=1100°C for EB-PBF samples and; (d) T=1000°C; (e) T=1050°C;; (f) T=1100°C for wrought samples.

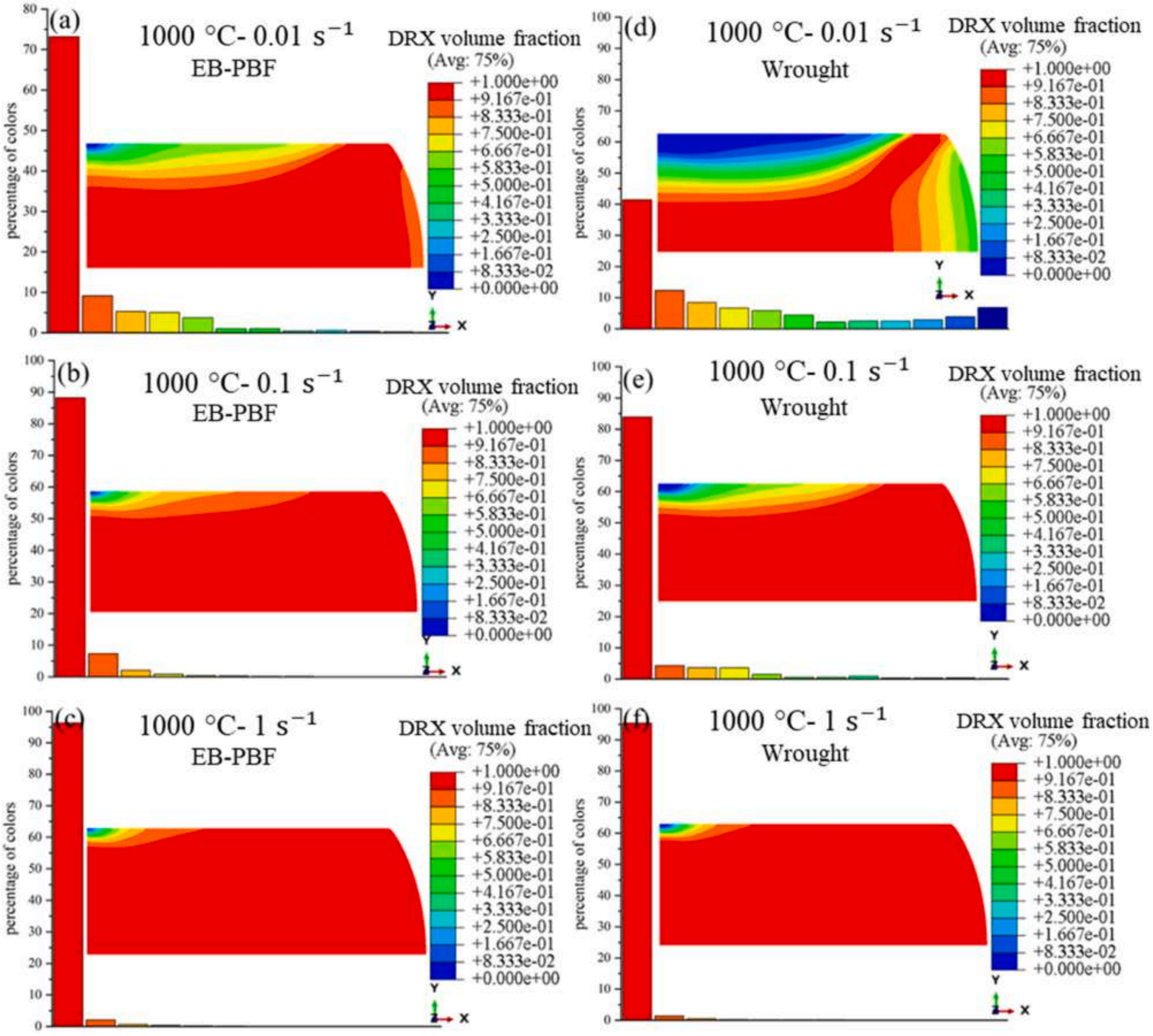

Fig. 15. DRX percentage distribution temperature of 1000°C and different strain rates: (a) $\dot{\varepsilon} = 0.01 s^{-1}$; (b) $\dot{\varepsilon} = 0.1\ s^{-1}$; (c) $\dot{\varepsilon} = 1 s^{-1}$ for EB-PBF samples, and (d) $\dot{\varepsilon} = 0.01\ s^{-1}$; (e) $\dot{\varepsilon} = 0.1 s^{-1}$; (f) $\dot{\varepsilon} = 1\ s^{-1}$ for wrought samples.

Table 2
Comparison of DRX volume fraction for the EB-PBF and wrought samples.

T (°C)	Strain rate (s-^{1})	X_{drx} for EB-PBF (%)	X_{drx} for wrought (%)
1000	0.01	96.30	95.46
1000	0.1	88.24	83.89
1000	1	73.17	41.41
1050	0.1	91.37	89.45
1100	0.1	93.77	92.45

EB-PBF samples is 88 % when subjected to a strain rate of 0.1 s^{-1} and a temperature of 1000 °C. In the same way, the recrystallisation ratio is 73 % at T=1000 °C and a strain rate of 1 s^{-1}. Moreover, the recrystallisation ratio reaches 91 % at T=1050 °C and a strain rate of 0.1 s^{-1}.

It can be concluded from the finite element (FE) simulation that as the strain rate decreases at a constant temperature, the volume fraction of recrystallised grains increases. Furthermore, with a constant strain rate, the proportion of recrystallised volume rises as the temperature increases. This trend is observed for both wrought and EB-PBF samples, which aligns with the experimental and research findings in previous research works [44,47]. Table 2 provides the simulated values of DRX volume fraction under different conditions for both wrought and EB-PBF samples, allowing for a comprehensive understanding of the DRX behavior in various scenarios.

Fig. 16 comparatively depicts the experimental and simulation results, where it can be observed that both approaches are in close agreement. In addition, the experimental and numerical analysis results demonstrate that the volume fraction of DRX in the EB-PBF samples is consistently higher than in wrought parts. This observation holds across various deformation conditions, as previously discussed. Furthermore, it is evident in simulation results that the difference in DRX volume fraction between EB-PBF and wrought samples becomes more pronounced as the temperature decreases and the strain rate decreases, as evidenced by the experimental results. In order to validate the JMAK equations identified in this study, the R-squared errors have been reported for EB-PBF as 0.998, 0.987, 0.962, and 0.999 at each step. Conversely, for wrought, the R-squared errors are reported as 0.997, 0.971, 0.974, and 0.997, respectively, in the numerical analysis. This information is presented in Figs. 8, 9, 12, and 13.

Numerical descriptions of the recrystallisation evolution histories for

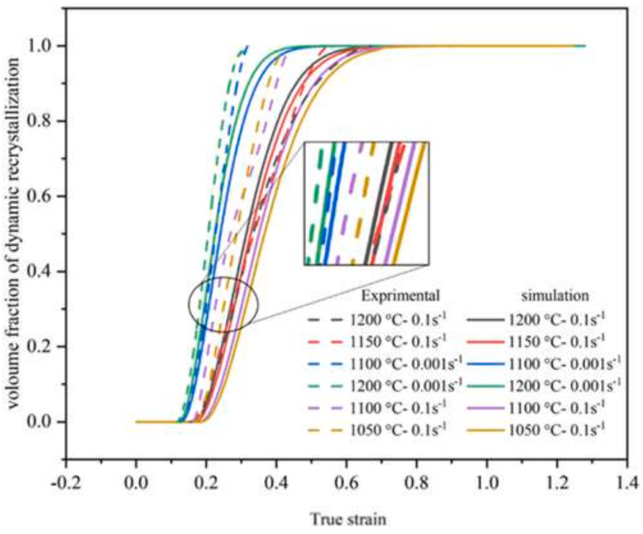

Fig. 16. Variation in the volume fraction of DRX for EB-PBF samples.

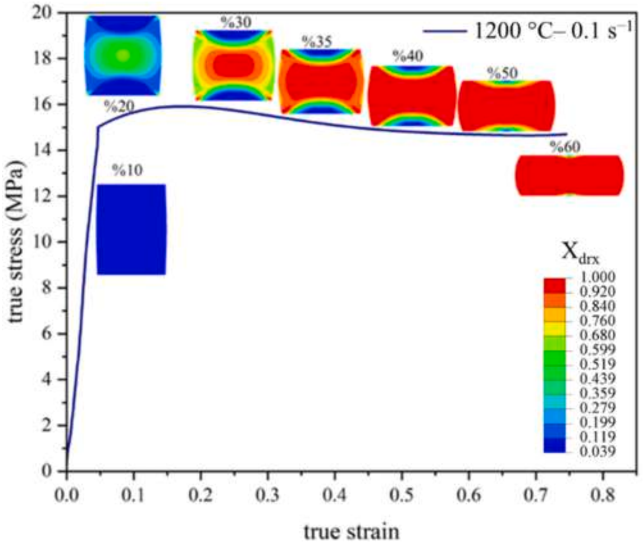

Fig. 17. The development and variation of the volume fraction of DRX related to the specimen subjected to different true strains at 1200 °C and 0.1 s^{-1} strain rate.

Ti64 alloy during hot forming processes can be obtained by employing finite element simulation (Fig. 17). Therefore, as a criterion in the design of the forming process for Ti64 alloy, ideal microstructures can be considered for DRX refinement to obtain improved mechanical properties. Consequently, the laborious process of trial and error can be avoided.

An examination of the microstructures of Ti64 specimens processed by EB-PBF after undergoing hot deformation in the single β region was conducted to validate the simulation outcomes further. Fig. 18 presents the typical microscopic images of a sample after the hot compression test in the single β region.

The investigation revealed the absence of localised shear bands across all evaluated samples post-hot compression. This observation aligns with the simulation predictions, which anticipated uniform DRX distribution. As documented in Fig. 18 (a), a notable barreling effect, a characteristic phenomenon associated with open-die forging, was evident, underscoring the mechanical response of the material under applied stress.

The analysed samples exhibited three different zones: a central zone undergoing severe plastic deformation (Zone 1), lateral zones experiencing partial plastic deformation (Zone 2), and a “dead” zone (Zone 3) located at the specimen end in contact with anvils. The dead zones (Zone 3) displayed no signs of microstructural transformations, suggesting an absence of restorative mechanisms during hot compression. This inactivity is attributed mainly to the localised heat dissipation and frictional interactions with the anvils.

Conversely, the central region of severe plastic deformation (Zone 1), detailed in Fig. 18(b) and (c), showcased noticeable disruptions in deformation features, likely due to cooling below the transit temperature. Within this zone, evidence of DRX, manifested through distorted prior β grain boundaries, was observed. Moreover, grains within this region appeared significantly elongated perpendicular to the direction of force application due to work-hardening and DRV processes during high-temperature deformation.

This microstructural investigation underscores the critical influence of initial structure, deformation conditions, and cooling rates post-deformation on microstructural evolution. Notably, the focus was directed towards the central zone of severe plastic deformation for its pivotal role in elucidating the mechanisms of hot deformation.

By tailoring the processing parameters and conditions, such as temperature, strain rate, and deformation history, it is possible to control and manipulate the occurrence and extent of DRX, ultimately leading to the desired microstructural characteristics. Instead of relying solely on experimental iterations, finite element simulation allows for a more efficient and targeted approach to achieve the desired mechanical properties by strategically inducing specific microstructural features through DRX refinement.

4. Conclusions

This work combines experimental, computational, and simulation approaches to comprehensively investigate the flow softening behaviour of EB-PBF and wrought Ti64 samples to highlight the integration of AM of Pre-forms and thermomechanical processing of metallic materials. The microstructural evolution and dynamic recrystallisation kinetics of Ti64 produced via EB-PBF at high temperatures have been studied and compared with its wrought counterpart. According to the findings, the following conclusion can be drawn:

- Friction-corrected stress-strain curves were analysed to understand flow softening behaviour, which is crucial for determining DRX initiation. It was observed that DRX occurred more rapidly in EB-PBF samples due to factors such as higher diffusion rates and the metastable microstructure resulting from rapid solidification.
- The results highlighted the influence of the manufacturing method on the DRX behavior, with EB-PBF samples exhibiting a faster flow softening behavior accompanied by higher DRX volume fractions.
- While the different flow softening behavior was alleviated at higher temperatures and lower strain rates of compression, the EB-PBF samples generally required lower critical stress and strain values to initiate DRX.
- Finite element simulation validated experimental findings, showing close agreement between experimental and simulated results in terms of DRX volume fractions. Simulation results indicated a consistently higher DRX volume fraction in EB-PBF samples compared to wrought samples under different deformation conditions.
- FEM results closely matched the experimental finding and hence are expected to provide valuable insights into microstructural evolution and offer a time-efficient alternative for process design and property optimisation, reducing the need for trial-and-error methods.
- The enhanced softening behavior can be linked to faster diffusion rates and higher SFE in the EB-PBF samples, thanks to the nonequilibrium circumstances of solidification and cooling during the EB-PBF process.

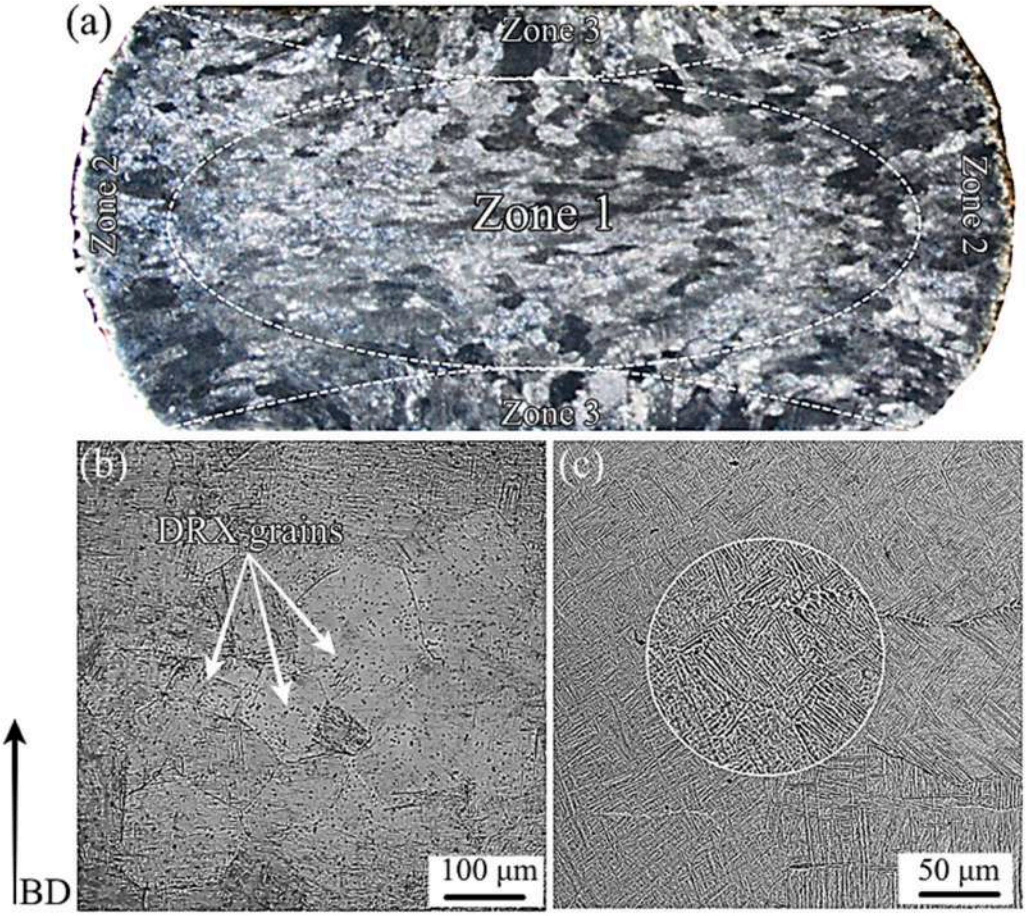

Fig. 18. (a) Macro image of EB-PBF Ti64 samples deformed at 1100°C/0.01 s^{-1}, (b) OM micrograph from Zone 1, and (d) SEM micrograph from Zone 1.

Overall, this study provides valuable insights into the dynamic recrystallisation behaviour of Ti64 alloy processed via EB-PBF, offering a systematic approach for optimising processing parameters to tailor microstructural characteristics and mechanical properties. Such understanding is crucial for advancing the integration of AM and conventional processing in producing high-performance metallic components. As a matter of fact, the findings of this paper enhance the understanding of Ti64 alloy thermomechanical behavior and add further flexibility to the supply chain of AM Ti64 products.

Funding

This research did not receive any specific grant from funding agencies in the public, commercial, or not-for-profit sectors.

CRediT authorship contribution statement

MohammadHossein Mosallanejad: Writing – review & editing, Validation, Formal analysis, Data curation. **Ata Abdi:** Writing – original draft, Investigation, Formal analysis. **Mohammad Taghian:** Writing – original draft, Investigation, Formal analysis, Data curation. **Hossein Mani:** Writing – original draft, Software, Formal analysis, Data curation. **Abdollah Saboori:** Writing – review & editing, Supervision, Investigation, Conceptualization. **Luca Iuliano:** Writing – review & editing, Supervision, Resources.

Declaration of Competing Interest

The authors declare that they have no known competing financial interests or personal relationships that could have appeared to influence the work reported in this paper.

Data availability

Data will be made available on request.

References

[1] H.J. Rack, J.I. Qazi, Titanium alloys for biomedical applications, Mater. Sci. Eng. C. 26 (2006) 1269–1277, https://doi.org/10.1016/j.msec.2005.08.032.

[2] L.C. Zhang, L.Y. Chen, A review on biomedical titanium alloys: recent progress and prospect, Adv. Eng. Mater. 21 (2019) 1–29, https://doi.org/10.1002/adem.201801215.

[3] F.A. Anene, C.N. Aiza Jaafar, I. Zainol, M.A. Azmah Hanim, M.T. Suraya, Biomedical materials: a review of titanium based alloys, Proc. Inst. Mech. Eng. Part C. J. Mech. Eng. Sci. 235 (2021) 3792–3805, https://doi.org/10.1177/0954406220967694.

[4] M. Sarraf, E. Rezvani Ghomi, S. Alipour, S. Ramakrishna, N. Liana Sukiman, A state-of-the-art review of the fabrication and characteristics of titanium and its alloys for biomedical applications, Bio-Des. Manuf. 5 (2022) 371–395, https://doi.org/10.1007/s42242-021-00170-3.

[5] M. Mohr, R. Wunderlich, R. Novakovic, E. Ricci, H.J. Fecht, Precise Measurements of thermophysical properties of liquid Ti–6Al–4V (Ti64) alloy on board the international space station, Adv. Eng. Mater. 22 (2020), https://doi.org/10.1002/adem.202000169.

[6] R. Elshaer, K. Ibrahim, Applications of titanium alloys in aerospace manufacturing: a brief review, Bull. Tabbin Inst. Metall. Stud. 111 (2022) 60–69, https://doi.org/10.21608/tims.2023.174504.1007.

[7] B. Farhang, A.A. Tanrikulu, A. Ganesh-Ram, S.H. Durlov, N. Shayesteh Moghaddam, Innovative fabrication design for in situ martensite decomposition and enhanced mechanical properties in laser powder bed fused Ti6Al4V alloy, J. Manuf. Mater. Process. 7 (2023), https://doi.org/10.3390/jmmp7060226.

[8] S.D. Castellanos, J.L. Alves, R.J. Neto, A comparative study of manufacturing processes of complex surface parts in Titanium Ti6Al4V, Ciência Tecnol. Dos. Mater. 29 (2017) 73–78, https://doi.org/10.1016/j.ctmat.2017.03.002.

[9] M. Jackson, K. Dring, Materials perspective: a review of advances in processing and metallurgy of titanium alloys, Mater. Sci. Technol. 22 (2006) 881–887, https://doi.org/10.1179/174328406X111147.

[10] I. Weiss, S.L. Semiatin, Thermomechanical processing of alpha titanium alloys, TMS Annu. Meet. (1998) 147–161.

[11] F. Meiners, J. Ihne, P. Jürgens, S. Hemes, M. Mathes, I. Sizova, M. Bambach, R. Hama-Saleh, A. Weisheit, New hybrid manufacturing routes combining forging and additive manufacturing to efficiently produce high performance components from Ti-6Al-4V, Procedia Manuf. 47 (2020) 261–267, https://doi.org/10.1016/j.promfg.2020.04.215.

[12] Z.Z. Fang, P. Sun, Pathways to optimize performance/cost ratio of powder metallurgy titanium - A perspective, Key Eng. Mater. 520 (2012) 15–23, https://doi.org/10.4028/www.scientific.net/KEM.520.15.

[13] L. Bolzoni, S. Raynova, F. Yang, An alternative method to manufacture Ti alloys from particulate materials, Powder Technol. 380 (2021) 341–348, https://doi.org/10.1016/j.powtec.2020.11.013.

[14] Y. Zhang, Z.Z. Fang, Y. Xia, Z. Huang, H. Lefler, T. Zhang, P. Sun, M.L. Free, J. Guo, A novel chemical pathway for energy efficient production of Ti metal from upgraded titanium slag, Chem. Eng. J. 286 (2016) 517–527, https://doi.org/10.1016/j.cej.2015.10.090.

[15] E.D. Herderick, Additive Manufacturing of Metals: A Review, in: 2011. ⟨https://api.semanticscholar.org/CorpusID:30006610⟩.

[16] F.I. Azam, A.M. Abdul Rani, K. Altaf, T.V.V.L.N. Rao, H.A. Zaharin, An in-depth review on direct additive manufacturing of metals, IOP Conf. Ser. Mater. Sci. Eng. 328 (2018), https://doi.org/10.1088/1757-899X/328/1/012005.

[17] A. Bandyopadhyay, Y. Zhang, S. Bose, Recent developments in metal additive manufacturing, Curr. Opin. Chem. Eng. 28 (2020) 96–104, https://doi.org/10.1016/j.coche.2020.03.001.

[18] P.W. Trimby, I. Anderson, K. Mehnert, J. Porter, J. Wheeler, Characterizing the influence of parent grain structures on the physical properties of additively manufactured Ti-64 alloys using EBSD, Microsc. Microanal. 27 (2021) 2674–2676. ⟨https://api.semanticscholar.org/CorpusID:236503479⟩.

[19] S. Megahed, V. Aniko, J.H. Schleifenbaum, Electron Beam-Melting and Laser Powder Bed Fusion of Ti6Al4V: transferability of process parameters, Metals 12 (2022), https://doi.org/10.3390/met12081332.

[20] H. Shipley, D. McDonnell, M. Culleton, R. Coull, R. Lupoi, G. O'Donnell, D. Trimble, Optimisation of process parameters to address fundamental challenges during selective laser melting of Ti-6Al-4V: a review, Int. J. Mach. Tools Manuf. 128 (2018) 1–20, https://doi.org/10.1016/j.ijmachtools.2018.01.003.

[21] T.S. Tshephe, S.O. Akinwamide, E. Olevsky, P.A. Olubambi, Additive manufacturing of titanium-based alloys- A review of methods, properties, challenges, and prospects, Heliyon 8 (2022) e09041, https://doi.org/10.1016/j.heliyon.2022.e09041.

[22] A. Malakizadi, D. Mallipeddi, S. Dadbakhsh, R. M'Saoubi, P. Krajnik, Post-processing of additively manufactured metallic alloys – A review, Int. J. Mach. Tools Manuf. 179 (2022) 103908, https://doi.org/10.1016/j.ijmachtools.2022.103908.

[23] R. Ding, Z.X. Guo, A. Wilson, Microstructural evolution of a Ti–6Al–4V alloy during thermomechanical processing, Mater. Sci. Eng. A. 327 (2002) 233–245, https://doi.org/10.1016/S0921-5093(01)01531-3.

[24] G.Z. Quan, Y.P. Mao, G.S. Li, W.Q. Lv, Y. Wang, J. Zhou, A characterization for the dynamic recrystallization kinetics of as-extruded 7075 aluminum alloy based on true stress-strain curves, Comput. Mater. Sci. 55 (2012) 65–72, https://doi.org/10.1016/j.commatsci.2011.11.031.

[25] G. Quan, G. Luo, J. Liang, D. Wu, A. Mao, Q. Liu, Modelling for the dynamic recrystallization evolution of Ti–6Al–4V alloy in two-phase temperature range and a wide strain rate range, Comput. Mater. Sci. 97 (2015) 136–147, https://doi.org/10.1016/j.commatsci.2014.10.009.

[26] A.M. Roy, R. Arróyave, V. Sundararaghavan, Incorporating dynamic recrystallization into a crystal plasticity model for high-temperature deformation of Ti-6Al-4V, Mater. Sci. Eng. A. 880 (2023) 145211, https://doi.org/10.1016/j.msea.2023.145211.

[27] A. Najafizadeh, J.J. Jonas, Predicting the critical stress for initiation of dynamic recrystallization, ISIJ Int 46 (2006) 1679–1684, https://doi.org/10.2355/isijinternational.46.1679.

[28] E.I. Poliak, J.J. Jonas, Initiation of dynamic recrystallization in constant strain rate hot deformation, ISIJ Int 43 (2003) 684–691, https://doi.org/10.2355/isijinternational.43.684.

[29] E.I. Poliak, J.J. Jonas, Critical strain for dynamic recrystallization in variable strain rate hot deformation, ISIJ Int 43 (2003) 692–700, https://doi.org/10.2355/isijinternational.43.692.

[30] C. de Formanoir, S. Michotte, O. Rigo, L. Germain, S. Godet, Electron beam melted Ti–6Al–4V: microstructure, texture and mechanical behavior of the as-built and heat-treated material, Mater. Sci. Eng. A. 652 (2016) 105–119, https://doi.org/10.1016/j.msea.2015.11.052.

[31] A. Saboori, A. Abdi, S.A. Fatemi, G. Marchese, S. Biamino, H. Mirzadeh, Hot deformation behavior and flow stress modeling of Ti–6Al–4V alloy produced via electron beam melting additive manufacturing technology in single β-phase field, Mater. Sci. Eng. A. 792 (2020) 139822, https://doi.org/10.1016/j.msea.2020.139822.

[32] M.A. Galindo-Fernández, K. Mumtaz, P.E.J. Rivera-Díaz-del-Castillo, E.I. Galindo-Nava, H. Ghadbeigi, A microstructure sensitive model for deformation of Ti-6Al-4V describing Cast-and-Wrought and Additive Manufacturing morphologies, Mater. Des. 160 (2018) 350–362, https://doi.org/10.1016/j.matdes.2018.09.028.

[33] A. Saboori, M. Pavese, S. Biamino, P. Fino, M. Lombardi, Determination of critical condition for initiation of dynamic recrystallisation in Zr-1%Nb alloy, J. Alloy. Compd. 757 (2018) 1–7, https://doi.org/10.1016/j.jallcom.2018.05.052.

[34] R. Ebrahimi, A. Najafizadeh, A new method for evaluation of friction in bulk metal forming, J. Mater. Process. Technol. 152 (2004) 136–143, https://doi.org/10.1016/j.jmatprotec.2004.03.029.

[35] A. Saboori, M. Dadkhah, M. Pavese, D. Manfredi, S. Biamino, P. Fino, Hot deformation behavior of Zr-1%Nb Alloy: Flow Curve Analysis and Microstructure Observations, Mater. Sci. Eng. A. 696 (2017) 366–373, https://doi.org/10.1016/j.msea.2017.04.049.

[36] E.I. Poliak, J.J. Jonas, A one-parameter approach to determining the critical conditions for the initiation of dynamic recrystallization, Acta Mater. 44 (1996) 127–136, https://doi.org/10.1016/1359-6454(95)00146-7.

[37] J.J. Jonas, X. Quelennec, L. Jiang, É. Martin, The Avrami kinetics of dynamic recrystallization, Acta Mater. 57 (2009) 2748–2756, https://doi.org/10.1016/j.actamat.2009.02.033.

[38] Z. Liu, D. Zhao, P. Wang, M. Yan, C. Yang, Z. Chen, J. Lu, Z. Lu, Additive manufacturing of metals: microstructure evolution and multistage control, J. Mater. Sci. Technol. 100 (2022) 224–236, https://doi.org/10.1016/j.jmst.2021.06.011.

[39] E. Alabort, P. Kontis, D. Barba, K. Dragnevski, R.C. Reed, On the mechanisms of superplasticity in Ti-6Al-4V, Acta Mater. 105 (2016) 449–463, https://doi.org/10.1016/j.actamat.2015.12.003.

[40] T. Seshacharyulu, S.C. Medeiros, J.T. Morgan, J.C. Malas, W.G. Frazier, Y.V.R. K. Prasad, Hot deformation mechanisms in ELI Grade Ti-6a1–4 V, Scr. Mater. 41 (1999) 283–288, https://doi.org/10.1016/S1359-6462(99)00163-3.

[41] R. Ding, Z. Guo, A. Wilson, Microstructural evolution of a Ti–6Al–4V alloy during thermomechanical processing, Mater. Sci. Eng.: A 327 (2) (2002) 233–245.

[42] M. Fanfoni, M. Tomellini, The Johnson-Mehl-Avrami-Kolmogorov model: A brief review (*), (1998) 7–8.

[43] M.K. Razali, M.S. Joun, A new approach of predicting dynamic recrystallization using directly a flow stress model and its application to medium Mn steel, J. Mater. Res. Technol. 11 (2021) 1881–1894, https://doi.org/10.1016/j.jmrt.2021.02.026.

[44] J.E. Burke, D. Turnbull, Recrystallization and grain growth, Prog. Met. Phys. 3 (1952) 220–292, https://doi.org/10.1016/0502-8205(52)90009-9.

[45] C.W. Price, Use of Kolmogorov-Johnson-Mehl-Avrami kinetics in recrystallization of metals and crystallization of metallic glasses, Acta Metall. Mater. 38 (1990) 727–738, https://doi.org/10.1016/0956-7151(90)90024-B.

[46] T. Matsui, T. Ogawa, Y. Adachi, Relationship between three-dimensional microstructure and Avrami exponent for recrystallization in pure iron, Results Mater. 1 (2019) 100002, https://doi.org/10.1016/j.rinma.2019.100002.

[47] C.H. Ng, M.J. Bermingham, M.S. Dargusch, Controlling grain size, morphology and texture in additively manufactured β-titanium alloy with super transus hot isostatic pressing, Addit. Manuf. 59 (2022) 103176, https://doi.org/10.1016/j.addma.2022.103176.